Sensor and Simulation Notes

Note 506

January 2006

**A Frequency Selective Surface Used as a Broadband Filter
to Pass Low-Frequency UWB while Reflecting X–Band Radar**

W. Scott Bigelow and Everett G. Farr
Farr Research, Inc.

J. Scott Tyo
University of New Mexico

William D. Prather and Tyrone C. Tran
Air Force Research Laboratory, Directed Energy Directorate

Abstract

Airborne ultra wideband (UWB) impulse-radiating antennas (IRAs) present an especially large radar cross section to X–band radar. To mitigate this problem, we have numerically and experimentally investigated the use of a frequency selective surface (FSS) as a broadband filter to reflect X–band radar while transmitting lower-frequency UWB signals without loss or dispersion. We present here results of numerical simulations and experimental measurements demonstrating an FSS that reflects essentially all of an X–band signal, but is transparent to UWB frequencies below 2.5 GHz.

1. Introduction

Airborne ultra wideband (UWB) systems often must use UWB antennas of various designs. These may include reflector Impulse Radiating Antennas (IRAs), TEM horns with or without lenses, and several others. Unfortunately, the broad bandwidth of these antennas causes them to present an especially large radar cross section, which is unsuitable in certain situations.

Here, we seek to conceal an IRA from X–band radar, while permitting it to perform its UWB mission. Typically, UWB systems operate in a frequency range below about 5 GHz, whereas typical radars operate at X–band, 8–12.4 GHz. To take advantage of this difference in operating frequencies, we identify a window or radome material that allows transmission of UWB signals below 5 GHz without dispersion. At the same time, the window must be highly reflective to X–band radar. Ideally, the material's reflective properties at X–band would be similar to those of the aircraft body, to eliminate any discontinuity in the surface properties.

To design our window, we use a frequency selective surface (FSS), consisting of a planar periodic array of conducting shapes. A complete window may contain multiple FSS layers. The UWB antenna is positioned behind the window, as shown in Figure 1. Although FSSs have been used extensively in radomes and other protective structures for narrowband applications, this UWB application is new, requiring both a broad, low-frequency, dispersion-less pass band and a similar high-frequency stop band.
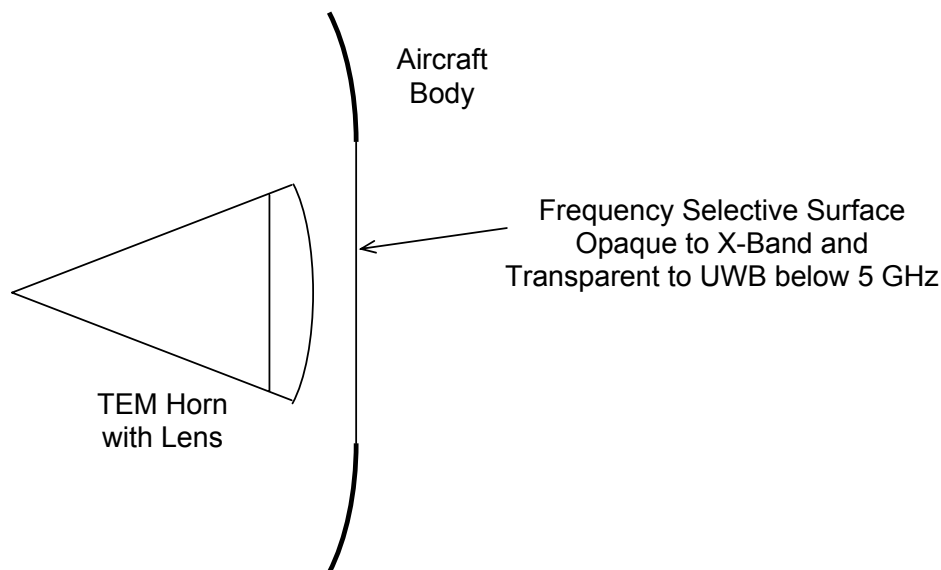

Figure 1. Concealment of an IRA (TEM horn with aperture lens) by an FSS window.

2. Modeling of Frequency Selective Surfaces for UWB Applications

Frequency selective surfaces can be thought of as passive electromagnetic filters. An FSS is typically composed of a periodic array of passive scattering structures of particular shape. Two classes of FSS can be distinguished based on whether the scatterers are apertures in a conducting screen or conducting objects arranged in a lattice. The former class of FSS is typically thought of as inductive, while the latter is thought of as capacitive. A schematic of complementary slot and dipole FSS structures is shown in Figure 2.
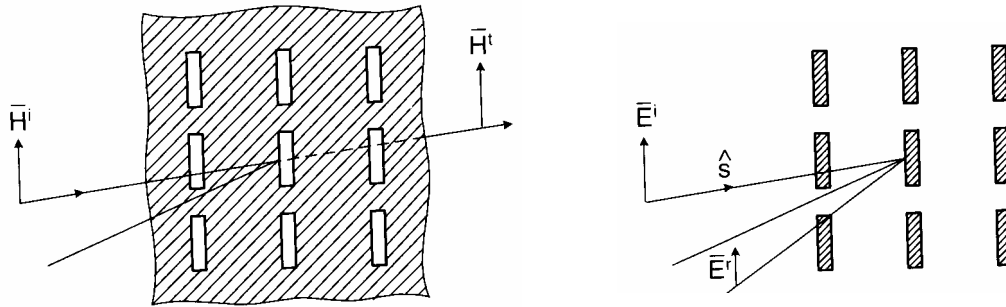

Figure 2. General schematic of inductive (left) and capacitive (right) screens arranged in complementary periodic lattices. The individual elements can resonate, as can the periodic structures. Based on Figure 1.3 of Munk [1, p. 4]

Though they are called frequency selective *surfaces*, in most applications, a full radome is composed of multiple layers of individual surfaces, providing 3-dimensional design capabilities. The basic operating principle of an FSS is that the individual elements can be made to resonate with specific frequency and polarization properties, the 2-dimensional periodic array can be made to resonate with its own frequency properties, and the multiple layers can interact and resonate. These multiple degrees of freedom can be exploited to design fairly complicated filters, including low-pass, high-pass, band-stop, and band-pass systems, depending on the application.

Frequency domain analysis of FSS structures is a very mature topic, beginning with a 1919 patent issued to Marconi for a reflector composed of a periodic surface [1, Ch. 1]. The field has developed in parallel with the development of frequency domain phased array antennas, and the modeling tools used to analyze FSSs have much in common with the tools used for active arrays. One of the best sources for information on the design and analysis of FSSs is the recent book by Ben A. Munk, *Frequency Selective Surfaces: Theory and Design* [1]. While FSSs have been thoroughly investigated for narrowband applications, our purpose is to use an FSS as a band-stop filter that allows UWB signals from an IRA to pass undistorted at frequencies below about 5 GHz, while acting as a perfect reflector for radar frequencies in the range of 8–20 GHz. The reason for this is to allow the IRA to function in its UWB capacity while altering the RCS of the host platform as little as possible.

Figure 3 shows an example of the reflection spectrum as computed by Munk for a typical FSS. As can be seen, there is a broad, flat stop band that reflects energy in the frequency range of

interest. Although the reflection is small at low frequencies, there is fine resonant structure that could significantly impact the phase of the transmitted signal. Since IRAs are often used for applications where high instantaneous peak power is necessary, we need to characterize the dispersion and resulting pulse distortion expected when an IRA is placed behind an FSS. The calculation presented in Figure 3 assumed an infinite periodic structure. For our application, the FSS might approximate an infinite structure at high frequencies, while at the low end of the pass band (~1 GHz), the FSS is expected to behave as a finite structure. For that reason, we will explore finite FSSs, and compare their performance for UWB applications to that predicted for the infinite structures.

$D_x = .6096$ cm
$D_z = .6896$ cm
Hexagon perimeter = 2.07 cm
Gap = .15 cm
Line Width = .0171 cm

Surface Profile

$\varepsilon_r = 2.2$ D = 20 mil

$\varepsilon_r = 2.2$ D = 20 mil

$D_x = .6096$ cm
$D_z = .6896$ cm
Hexagon perimeter = 2.07 cm
Gap = .15 cm
Line Width = .0171 cm

Surface Profile

$\varepsilon_r = 2.2$ D = 20 mil

$\varepsilon_r = 2.2$ D = 20 mil

$\varepsilon_r = 1.4$ D = 1.4 cm

$\varepsilon_r = 2.2$ D = 20 mil
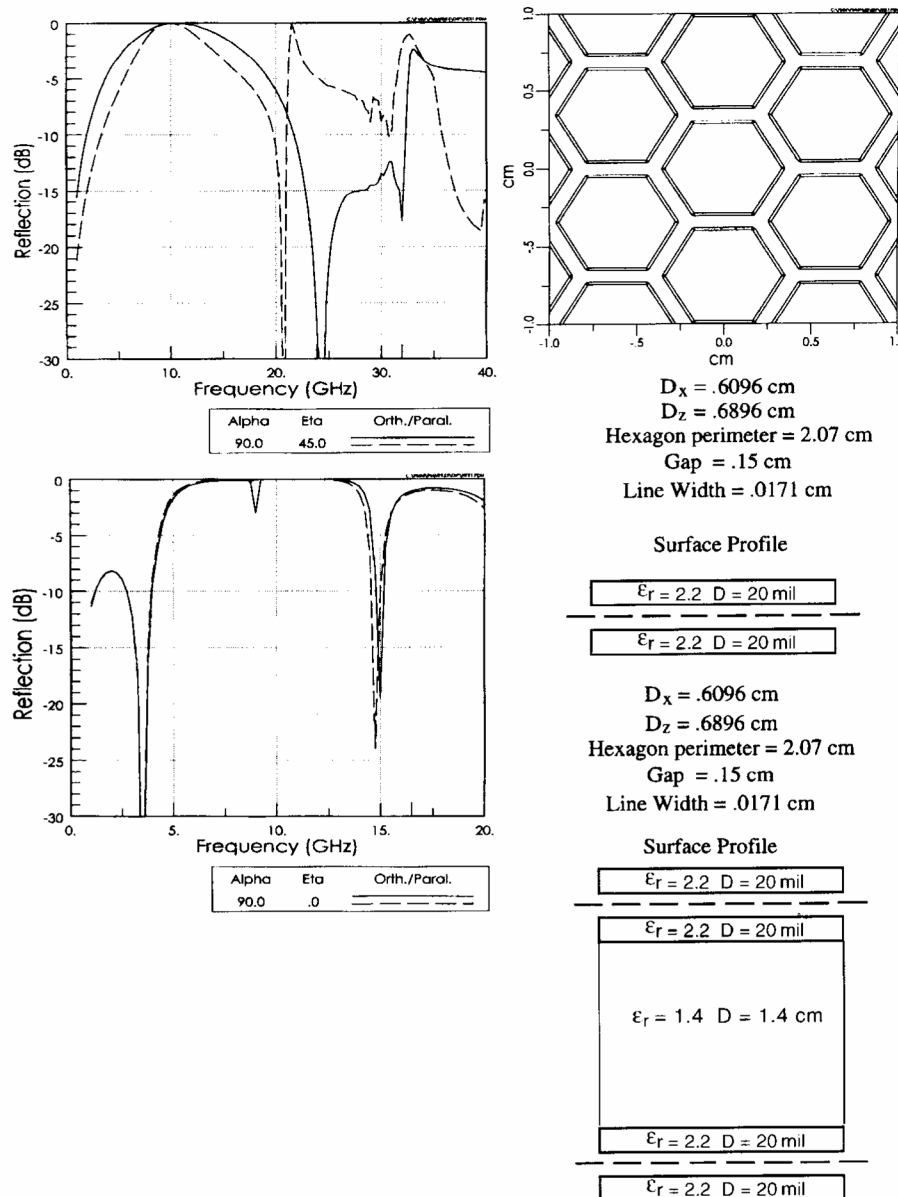
$\varepsilon_r = 2.2$ D = 20 mil

Figure 3. Typical multi-layer FSS lattice structure. The lattice is a hexagonal array meant to allow high transmission below about 5 GHz and high reflection from 7–15 GHz. This FSS consists of a cascade of two resonant periodic structures separated by dielectric materials. The assumption is that the actual FSS structures will be printed on and layered between typical circuit board materials. Figure 8.9 from Munk [1, p. 292].

4

FSSs and other periodic planar structures are typically modeled in the frequency domain using a technique known as the periodic method of moments. The brief description here can be supplemented by consulting the references [e.g., 1, Ch. 3 and 4]. Consider a scattering element of length $d\ell$ in direction $\hat{\mathbf{p}}$ as shown in Figure 4. The element is arranged as part of an infinite array with periodicity D_x in the x-direction and D_z in the z-direction. The incident plane wave is propagating in the direction,

$$\hat{\mathbf{s}} = s_x\hat{\mathbf{x}} + s_y\hat{\mathbf{y}} + s_z\hat{\mathbf{z}}. \tag{1}$$
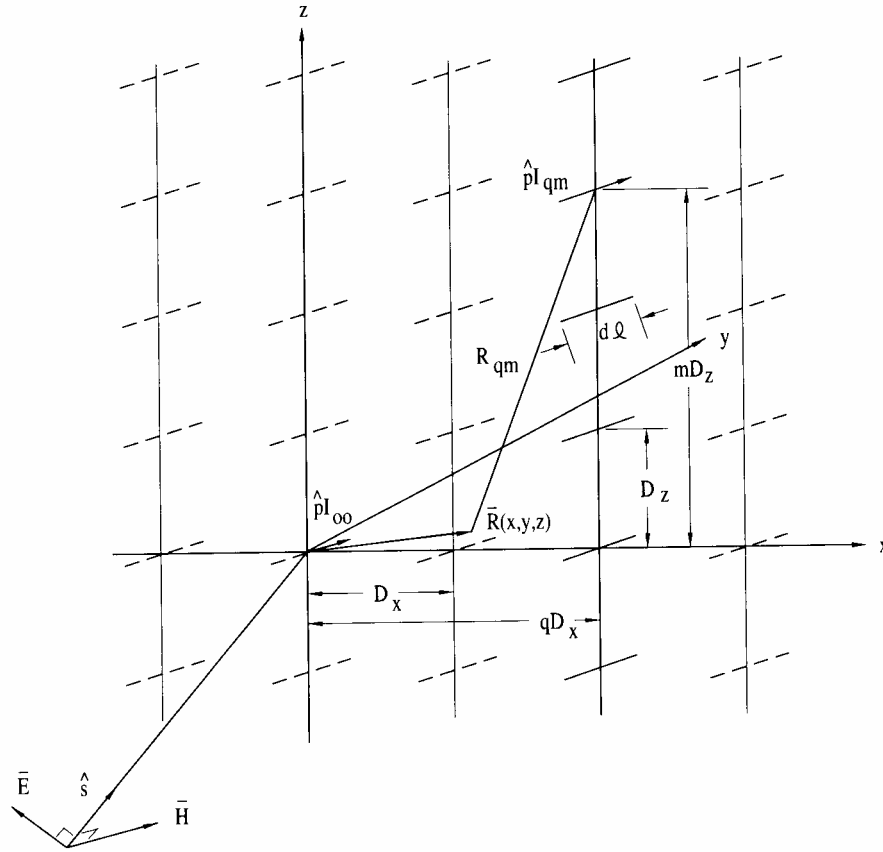
Figure 4. Scattering from an array of identical current elements. Figure 4.1 from Munk [1, p. 80].

Since we will consider only normal incidence in our analyses, we have $\hat{\mathbf{s}} = \hat{\mathbf{y}}$. In reality, when the FSS is in the near field of the antenna, other incident directions must also be considered. Furthermore, since most radomes are constructed as approximately spherical enclosures, an FSS laid out on the surface will likely be spherical instead of planar.

The induced current on the element at location q and m in the lattice, I_{qm}, produces a scattered magnetic vector potential

$$dA_{qm} = \hat{\ell} \frac{\mu d\ell}{4\pi} I_{qm} \frac{e^{-j\beta R_{qm}}}{R_{qm}}, \tag{2}$$

where R_{qm} is the distance from the element to the observer and β is the free space propagation constant. The total vector potential at the observation position is obtained by summing over all elements in the array as

$$dA = \hat{\ell} \frac{\mu d\ell}{4\pi} \sum_{m=-\infty}^{\infty} \sum_{q=-\infty}^{\infty} I_{qm} \frac{e^{-j\beta R_{qm}}}{R_{qm}}, \tag{3}$$

and the induced current is

$$I_{qm} = I_0 e^{-j\beta(mD_z s_z + qD_x s_x)}, \tag{4}$$

where I_0 is the magnitude of the induced current and the phase is assumed to have the same variation as the incident plane wave. In the case of normal incidence (4) becomes $I_{qm} = I_0$. The double sum in (3) can be evaluated through two uses of Poisson's sum formula [1, p. 82]. The resulting sum is

$$dA = \hat{\ell} \frac{\mu I_0 d\ell}{2j\beta D_x D_z} \sum_{k=-\infty}^{\infty} \sum_{n=-\infty}^{\infty} e^{-j\beta z\left(s_z + n\left(\frac{\lambda}{D_z}\right)\right)} e^{-j\beta x\left(s_x + k\left(\frac{\lambda}{D_x}\right)\right)} \frac{e^{-j\beta y\sqrt{1-\left(s_x + k\left(\frac{\lambda}{D_x}\right)\right)-\left(s_z + n\left(\frac{\lambda}{D_z}\right)\right)}}}{\sqrt{1-\left(s_x + k\left(\frac{\lambda}{D_x}\right)\right)-\left(s_z + n\left(\frac{\lambda}{D_z}\right)\right)}}. \tag{5}$$

Equation (5) is simply a sum over plane-wave modes, only a small number of which are propagating. However, the evanescent modes are still important, as they will contribute to element-to-element interactions. Once we have constructed (5), we can write down the induced electric and magnetic fields and apply standard moment method techniques to integrate $d\hat{\ell}$ over the unit cells[†] of the periodic array. Equation (5) can easily be modified to deal with a skewed grid, i.e., a grid whose 2-dimensional periodicity is in directions that are not necessarily orthogonal, such as a hexagonal array.

[†] The integration is only over one unit cell, the sum in (5) takes care of the periodic array.

3. Numerical Analyses for Normal Incidence

The designs investigated here come from Chapter 8 of Munk's text [1]. We focus on the band-stop filter designs, and our effort is to create filters (FSSs) that have very high reflection coefficients for high frequencies (especially frequencies near X–band, 8–12 GHz), while having high transmission at lower frequencies where an IRA might be expected to operate. For the analyses presented here, the periodic moment method was carried out using Zeland's IE3D commercial software package [2].

The first design we simulated is shown in Figure 3, and is taken from Figure 8.9 of Munk. It involves hexagonal loops separated by a uniform 0.15-cm gap. Figure 3 also shows Munk's predicted reflection from this structure. This structure is promising because it has high reflectivity beginning at about 6.5 GHz and extending through the X–band, with a null around 15 GHz. In the pass band, however, we see a resonant null and significant structure. Upon seeing this, we decided to focus on the phase of the transmitted signal to ensure that the time-domain waveform would be minimally distorted upon transmission.

The unit cell for the IE3D calculation is shown in Figure 5 and Figure 6. The details of the geometry are described in the captions of these figures. IE3D computes the scattering from finite structures only, so we sized our FSS to be a 10-wavelength square at 1 GHz. This is a much larger FSS than would be used in a real application. We performed analysis for normal incidence (though other angles could equally well have been simulated), and the results are presented in Figure 7. We see a relatively flat pass band with a few small resonances through the frequency range of interest. The performance is similar to that predicted by Munk. The differences are likely due to the finite size of the structures setting up incomplete resonances.
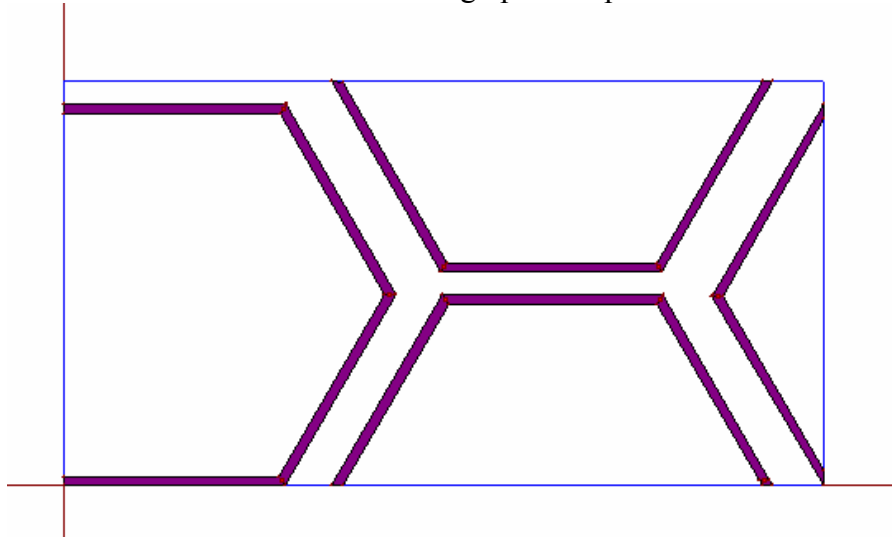

Figure 5. Unit cell for the IE3D calculations, showing a top view of the structure. There are actually two layers of hexagons, as shown in Figure 6, below. The geometry is taken from Figure 8.9 of Munk [1]. The perimeter of these equilateral hexagons is 2.07 cm, and the gap spacing is 0.15 cm. The unit cell is 1.185 cm × 0.635 cm. To compute the scattering, 40 cells were used in the horizontal direction and 80 in the vertical.
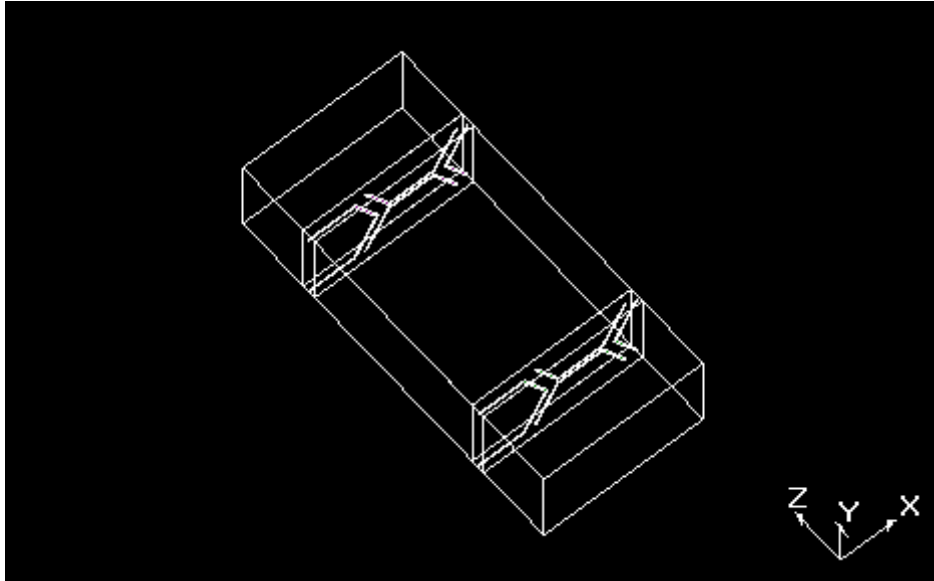
Figure 6. 3–D view of the IE3D unit cell. This cell simulates a two-layer FSS structure. The actual FSS lattices are each in the center of a pair of 0.0508-cm-thick dielectric sheets with $\varepsilon_r = 2.2$. The two FSS layers are separated by a 1.4-cm-thick slab of dielectric with $\varepsilon_r = 1.4$.
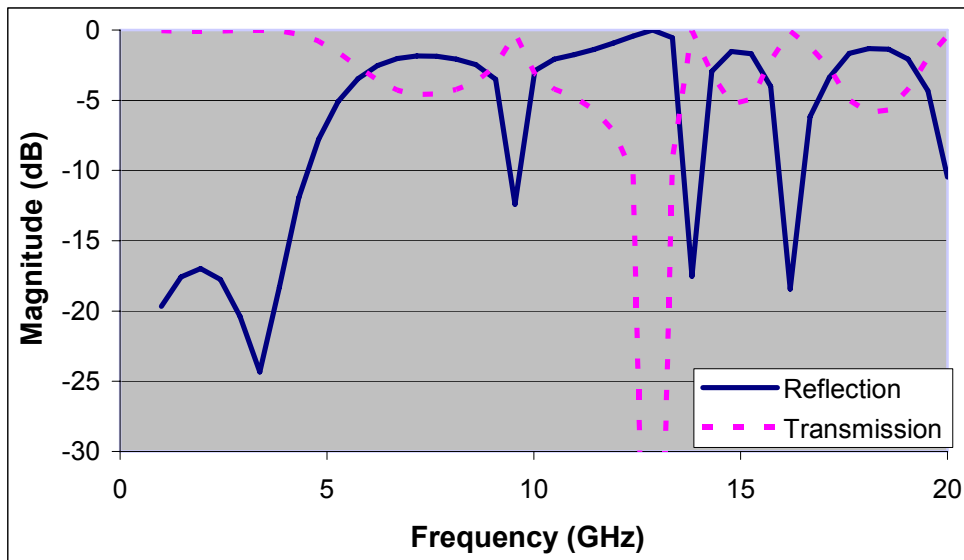

Figure 7. RCS calculation in the backscatter direction (equivalent to reflection). Only the reflection was directly computed, the transmission was determined using conservation of energy.

A final point of interest involves the amplitude and phase of the reflection and transmission in the pass band. For UWB use, we would like this to be completely flat in both amplitude and phase. Figure 8 shows the amplitude of the reflected and transmitted *scattered* field. Figure 9 shows the phase of the reflected signal (0°) and the transmitted signal (180°).
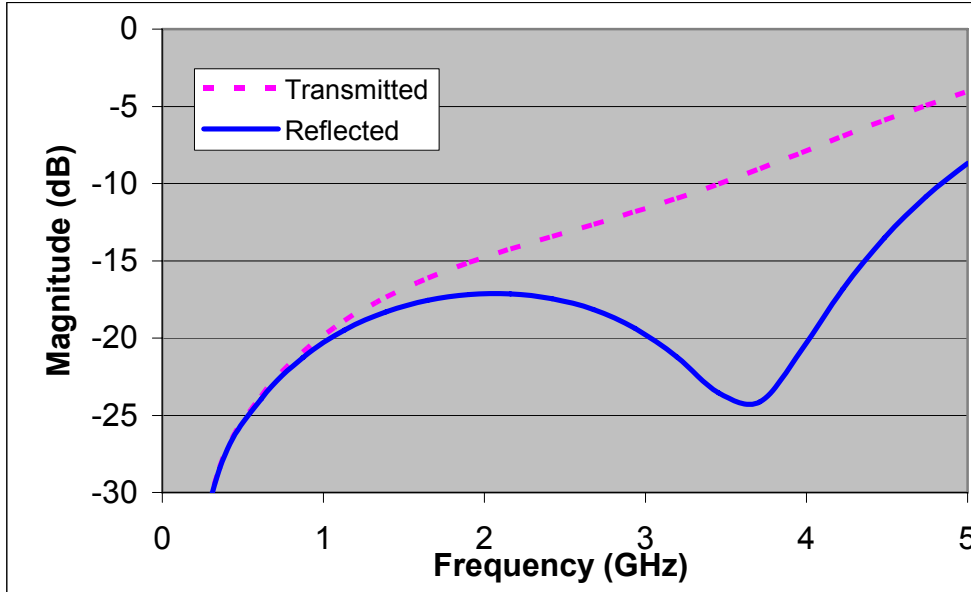
Figure 8. Magnitude of the transmitted and reflected signal from the structure pictured in Figure 6. The total transmitted field is the sum of the transmitted signal and the incident field (unit amplitude plane wave).
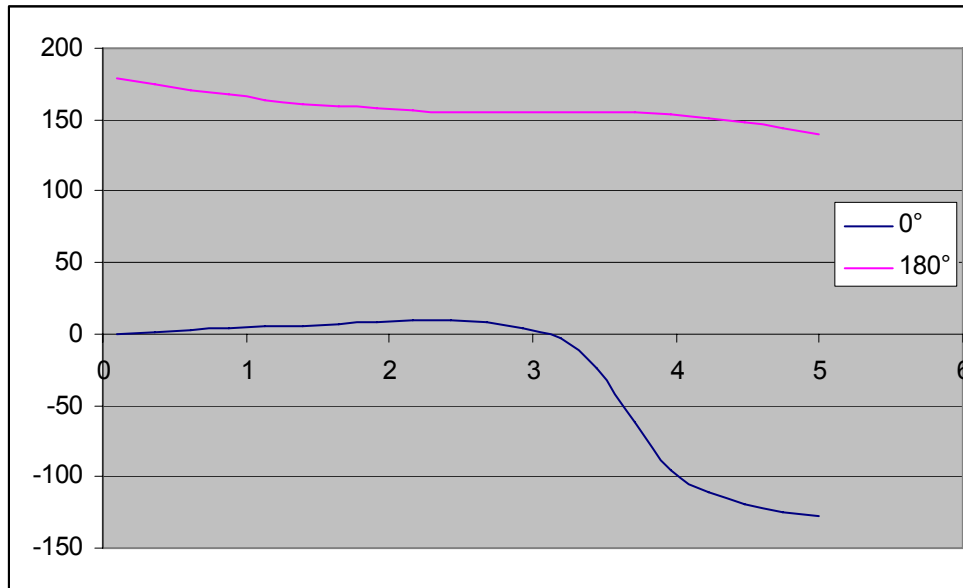

Figure 9. Phase angle in degrees of the reflected (0°) and transmitted (180°) *scattered* signals as a function of frequency from 100 MHz through 5 GHz. The total transmitted field is the sum of the transmitted scattered field and the incident field. Since the scattered field is ~15 dB down at these low frequencies (see Figure 8), we expect minimal distortion of the signal.

To compute the total transmitted signal, we construct a filter in the frequency domain that adds the "scattered" field at 180° to a unit plane wave and use this to filter the incident waveform. For argument's sake, we assume a Gaussian pulse with a 150-ps pulse width as the exciting signal. This has a 10 dB bandwidth of about 2 GHz. From Figure 10, which shows the original signal (blue) and the transmitted signal (red), we see that this filter provides the possibility of

having an ultra wideband, low-dispersion band-pass filter (FSS) for concealing an IRA. It is important to note that this assumes plane wave excitation, and does not include potential interactions that may occur if the FSS is in the near field of the IRA. The results presented in Figure 10 indicate that the pass band structure of the FSS is relatively distortion-free. This result is in keeping with results observed for wire-grid polarizers integrated with IRAs to control aperture polarization [3, 4]. Since we know that the FSS will work with the IRA for transmitting in the pass band, our remaining task is to find a geometry that provides a flatter structure in the stop band. Such a design is presented in the next section.
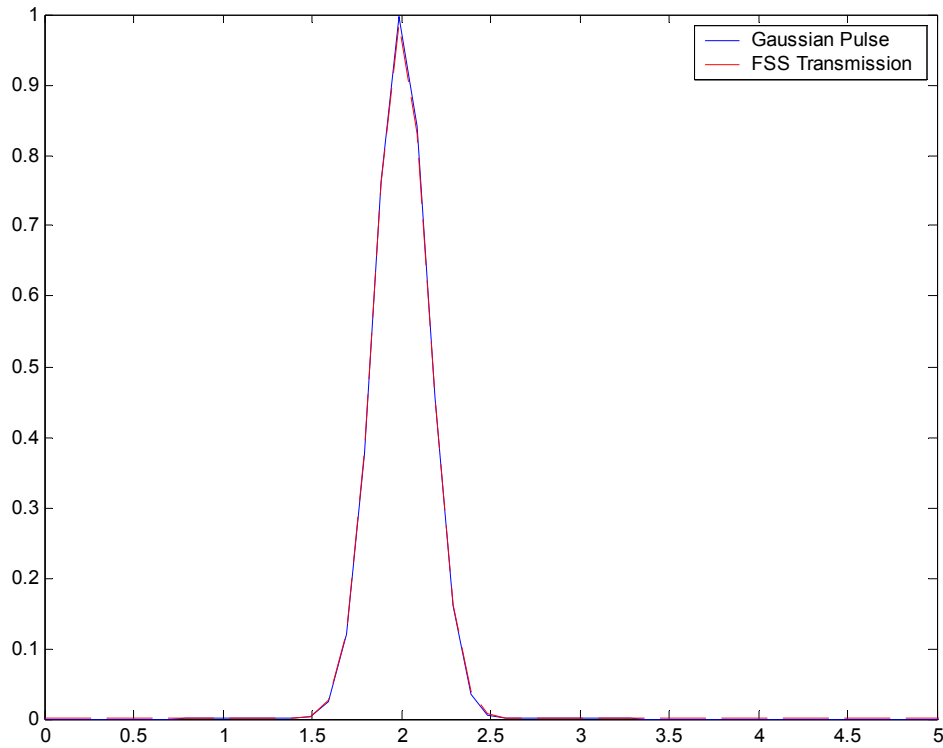

Figure 10. Incident plane wave Gaussian pulse with 150-ns standard deviation overlaid with the pulse transmitted through the FSS described above. This FSS provides minimal distortion of the radiated waveform.

4.   Experimental Realization and Measurement of a Frequency Selective Surface

Based on the extent of agreement between our simulations and those of Munk [1, Figure 8.9], we concluded that a somewhat different FSS design described by Munk (his Figure 8.12) would form the best basis for our application. Although that design includes outer dielectric matching layers, we eliminated that refinement for the current effort, leaving us with a design similar to that in Munk's Figure 8.11. Our chosen FSS pattern, shown in Figure 11, was etched on a 0.0508-cm (20-mil) RT/duroid 5880 sheet, clad with a single ½ oz/ft^2 copper foil layer. A single FSS layer was formed by overlaying the pattern with an unclad RT/duroid sheet, as indicated in Figure 12. A cascaded pair of FSS layers was formed by sandwiching a one-inch (2.54-cm) thick polystyrene foam block ($\varepsilon_r = 1.0$) between two single FSS layers. The block
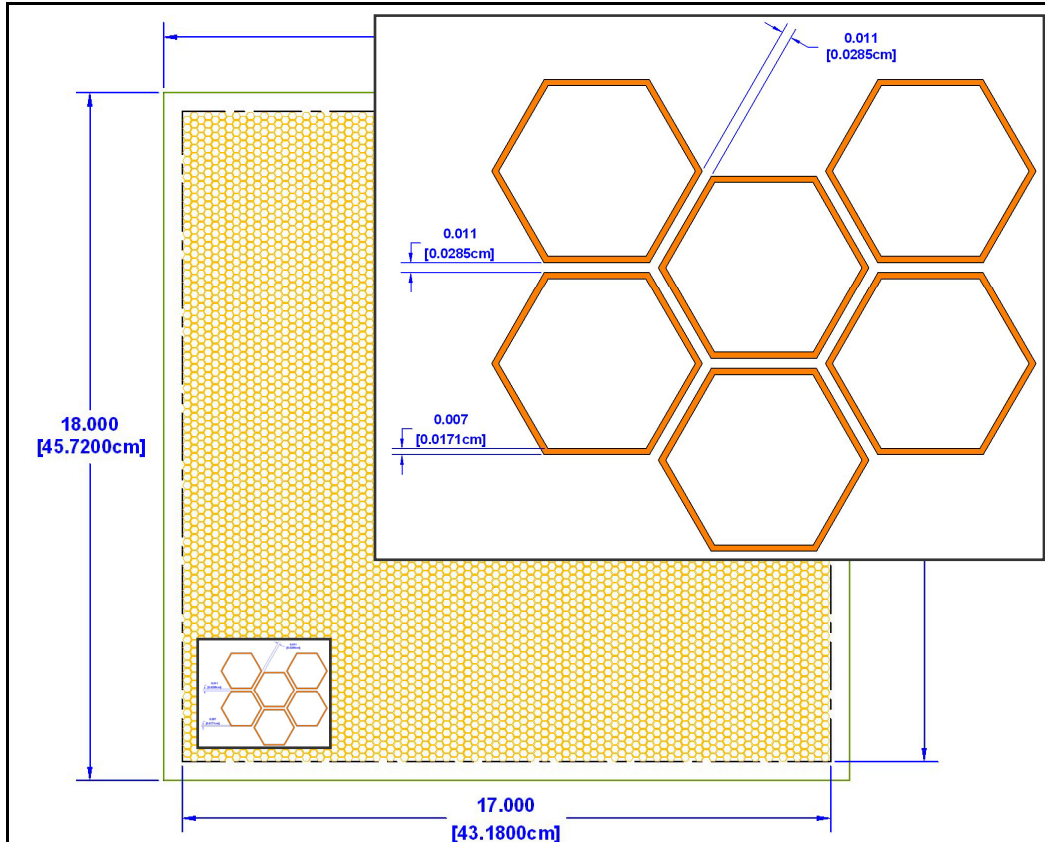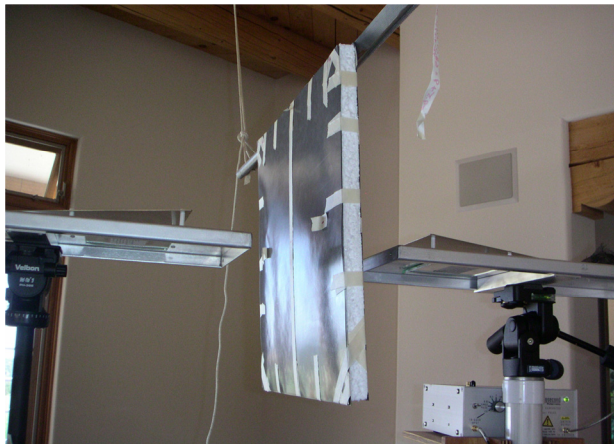
10

Figure 11. FSS pattern shown at scales of 1:5, 1:1 (small inset), and 5:1 (large inset). The perimeter of each hexagon is 1.71 cm and the gap between hexagons is 0.0285 cm, as shown in Figure 8.12 of [1].

Figure 12. Measurement setup (photo) and profiles (not drawn to scale) for a single FSS (left) and cascaded FSS pair (right).

differs from that used in Munk's Figure 8.11 and 8.12 in both thickness and dielectric constant. Also, the 2.54-cm thickness is considerably greater than the ideal layer separation for a dielectric constant of 1.0, specifically, 1.7 cm, or $\lambda/2$ at the center of the stop band. This alteration may cause some shift of resonances toward lower frequencies, as described by Munk [1, p. 289].

For measurement, the FSS structures were centered on and approximately normal to the boresight axis, midway between a pair of Farr Research TEM-1-50 horn antennas, as shown in Figure 12. The horn apertures were separated by 37 cm, and the horn ground planes were separated by 20 cm. The transmitting horn was fed by the 4-volt fast step output of a Picosecond Pulse Labs model 4015C pulser. The received signal was sampled by a Tektronix model 80E04 sampling head driving a model TDS8000B digital sampling oscilloscope. A 10-ns time window provided 4000 samples, and 1000 such records were averaged for each waveform measurement.

The measurement setup leads to inclusion in the data of multiple reflections between antennas and between antennas and FSS surfaces, as may be observed in the raw time-domain FSS response data of Figure 13. Although a large separation between FSS and antenna would minimize multiple reflections, unfiltered contributions arising from diffraction of signals at the perimeter of the FSS structure would then contaminate the measurements. Since our contemplated application will force the FSS surfaces into close proximity with the antenna we seek to conceal, we accept the reflections. Later, we use time gating to remove most reflection effects from our analyses.

To obtain the transmission response for either single or cascaded FSS layers, we first obtained the response of the pair of TEM horns with no FSS structure present (top pair of graphs in Figure 13). Then, we deconvolved that measurement from the response observed with the chosen FSS structure suspended between the horns (middle or bottom pair of graphs in Figure 13). The result is like a transfer function for transmission through the FSS structure.
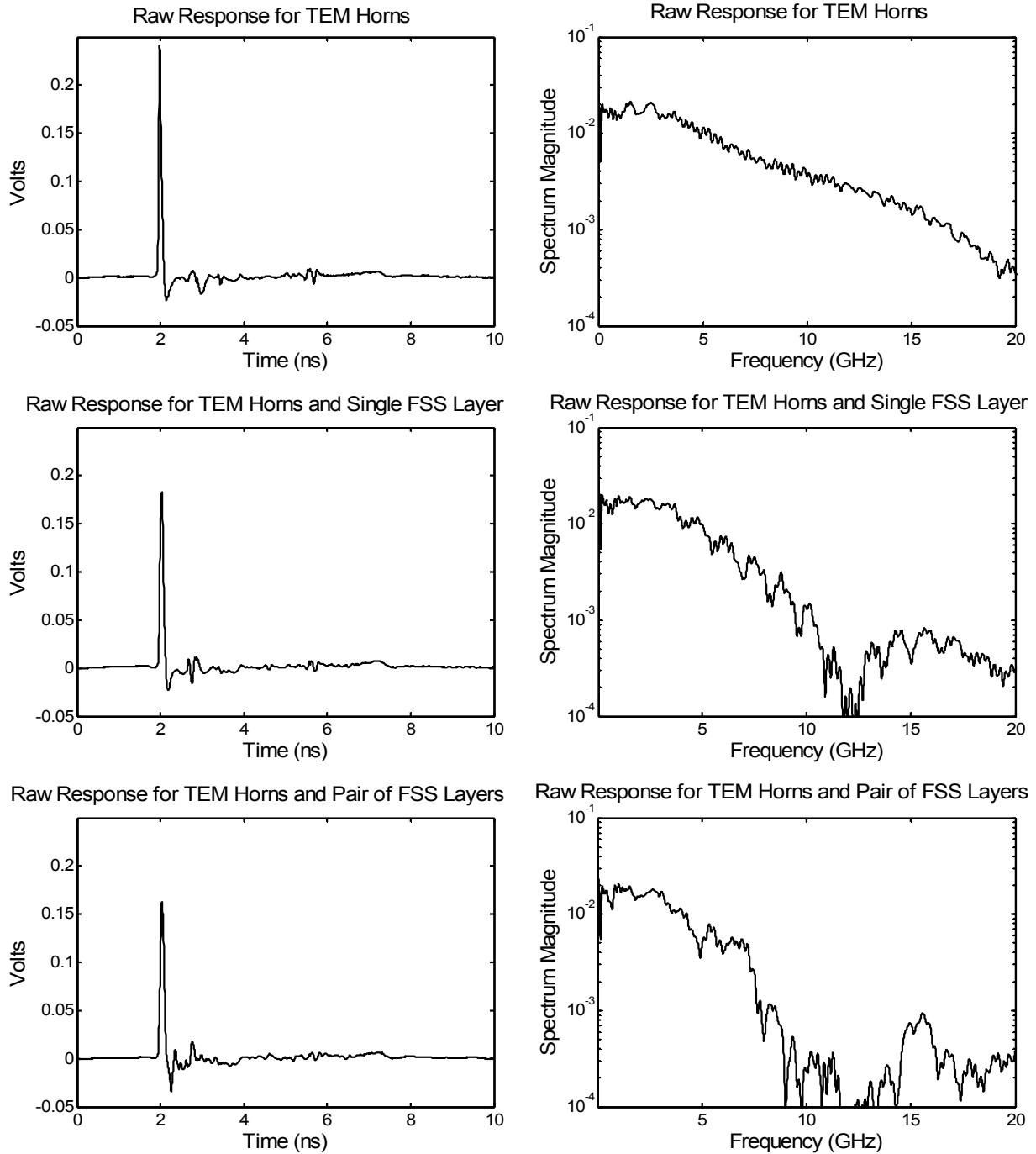
Figure 13. Raw impulse response measurements (left) and corresponding spectra (right) for a pair of TEM horn antennas (top), for the antennas with an intervening single FSS layer (middle), and with a cascaded pair of FSS layers (bottom).

We present the FSS response results, obtained as described above, in the graphs shown in Figure 14 and Figure 15. The upper pair of graphs in each figure shows the transmission magnitude and corresponding reflection for the FSS structure; the lower pair shows the phase of

the transmission response. The graphs on the left in each figure include the perturbing effects of multiple reflections. For the graphs on the right, time gating was used to eliminate most multiple reflections—those calculations used only up to the first 0.4 ns after arrival of the impulse maxima.
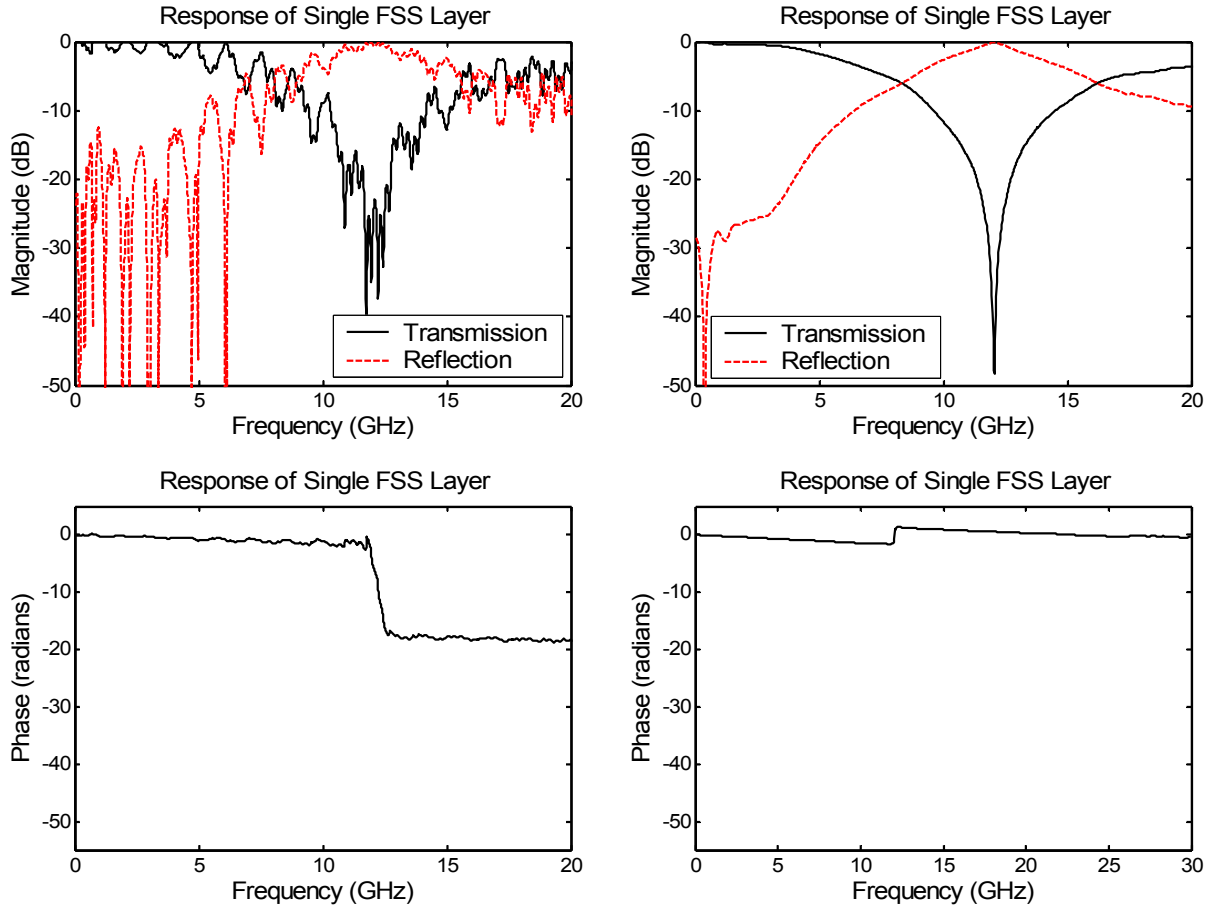

Figure 14. Transmission, reflection, and phase for the impulse response of a single FSS layer. Measurements in the right pair of plots were windowed in the time domain to exclude multiple reflections.
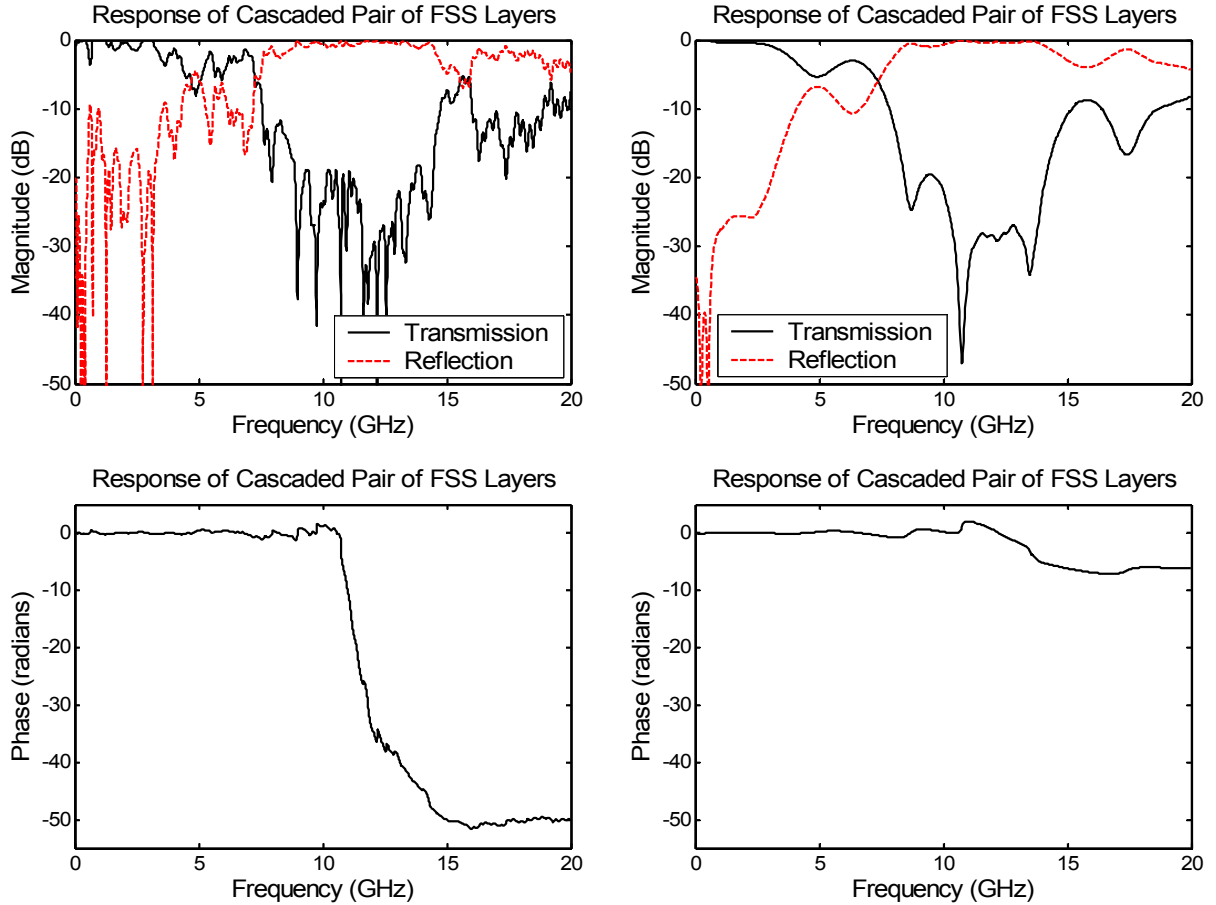
Figure 15. Transmission, reflection, and phase for the impulse response of a cascaded pair of FSS layers. Measurements in the right pair of plots were windowed in the time domain to exclude multiple reflections. The pass band extends up to about 3 GHz, and the stop band extends from about 8–14 GHz. The phase is essentially constant up to the start of the stop band.

5.   Comparison of Experimental Results with Numerical Simulations

We have no FSS simulations from Munk for either single FSS or cascaded FSS structures that exactly match our structures and measurement configurations [1]. For the single FSS case, this arises because Munk reports reflection curves only at 45° of incidence, whereas all our measurements were obtained at 0°. As noted above, for the cascaded FSS, we used a spacer material with different thickness and dielectric constant than those used by Munk. Finally, recall that all of Munk's simulations assume infinite FSS structures, while our design is finite. For all of these reasons, we rely most heavily on our own IE3D simulation of our FSS geometry for confirmation of our measurements.

IE3D simulations of FSS transmission and reflection corresponding to the measurements shown in Figure 14 and in Figure 15 are compared with those measurements in Figure 16. For the single FSS layer, we find major differences in the form of the frequency response, for which we have no explanation. In contrast, the results for the cascaded pair of FSS layers agree both in

general form and approximate magnitude. The major differences are in the width and depth of the resonances. In the measurement, the resonances are weaker and broader, but they occur at approximately the same frequencies as in the simulation. We also note that the simulation for this cascaded FSS design, with its tightly packed hexagons (0.0285-cm gap), agrees qualitatively with our earlier simulation for a more loosely packed design (0.15-cm gap, Figure 7 and Figure 9). The magnitude spectra are similar and the phase is nearly constant below the stop band.
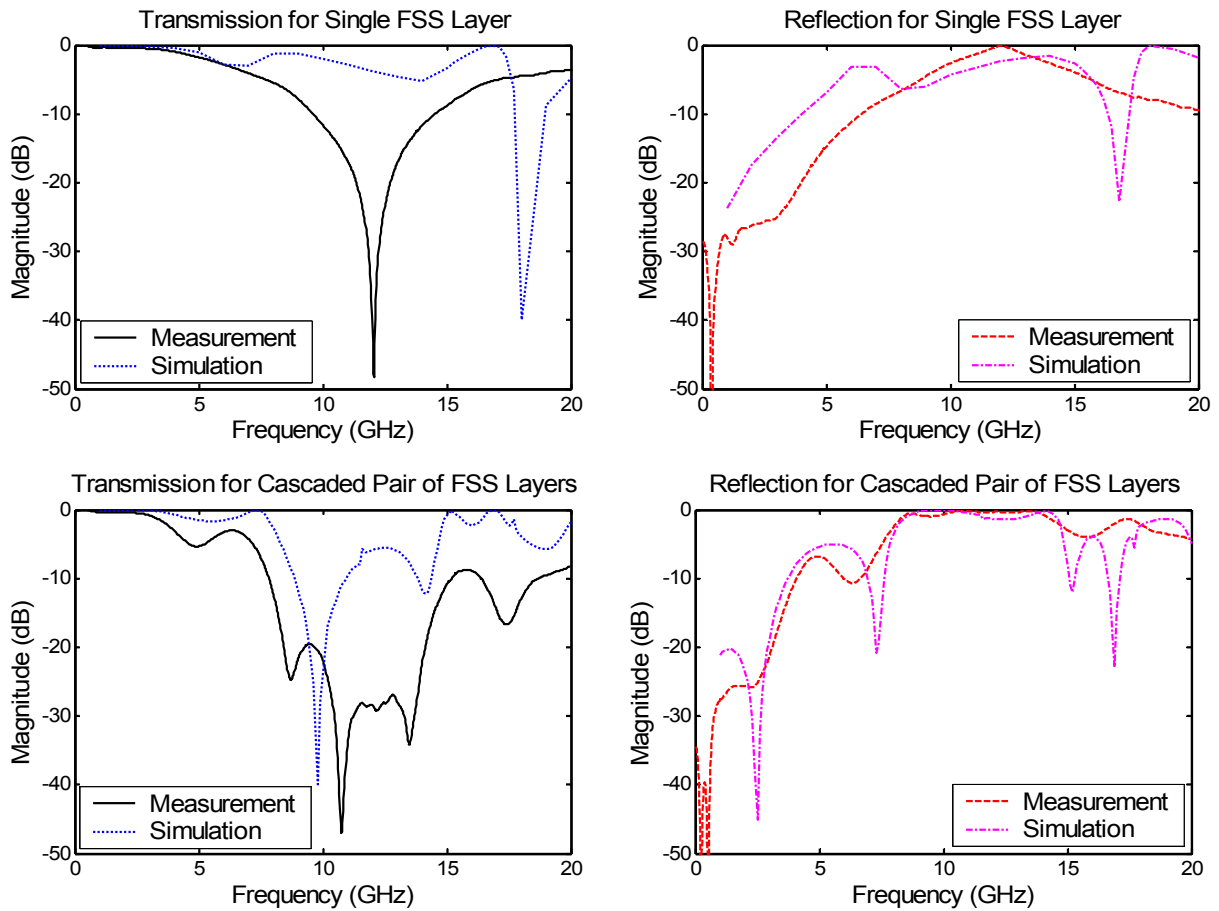

Figure 16. Comparison of measurements with IE3D predictions of the performance of one- and two-layer FSS structures.

6. Concluding Remarks

In this effort we have adopted, tested, and modeled a design for a cascaded two-layer band-stop FSS filter suitable for concealing a focused UWB antenna from X–band radar, while transmitting low-frequency UWB signals without loss or dispersion. In the stop-band we observed almost total reflection of X–band signals. In the pass-band, the phase of the transmitted UWB signal was essentially constant, and below 2.5 GHz, there was little attenuation. Based on this, we know that we can propagate low-frequency UWB signals through the FSS with little dispersion. Although this FSS has not yet been fully optimized, its measured performance agrees with our numerical simulations and it generally performs as desired.

Future work might encompass a number of areas. First, we note that we have simulated the FSS structure only for a normally incident plane wave. So future simulations should include other angles of incidence. Second, we note that although the measurements were nominally for a normally incident plane wave, they were, in fact, made with the FSS in the near field of both transmit and receive antennas. Future experimental FSS characterizations should investigate FSS performance for better-controlled configurations. Third, to improve performance in the stop band, the FSS should be constructed with a central dielectric spacer block having the ideal $\lambda/2$ thickness at the center of the stop band. Finally, since Munk's work has shown that the addition of outer matching dielectric layers can reduce the pass band attenuation [1, Figure 8.12]; such geometries should be investigated to further optimize FSS performance.

References:

1. B. A. Munk, *Frequency Selective Surfaces: Theory and Design*, John Wiley & Sons, New York, 2000.
2. Zeland Software, http://www.zeland.com/ie3d.html.
3. J. S. Tyo, C. J. Buchenauer, and J. Boddeker, "Improvement of Aperture Efficiency in Impulse Radiating Antennas by Polarization Control," 2004 IEEE Antennas and Propagation International Symposium, Monterey, CA, June 2004.
4. J. S. Tyo, M. Dogan, J. Boddeker, and C. J. Buchenauer, "Enhancing Aperture Efficiency of IRAs through Polarization Control of the Aperture Fields," accepted for publication in *IEEE Transactions on Antennas and Propagation*, July 2005.